

# Earth's albedo and its symmetry

George Datsseris<sup>1</sup> and Bjorn Stevens<sup>1</sup>

<sup>1</sup>Max Planck Institute for Meteorology

November 23, 2022

## Abstract

The properties of Earth's albedo and its symmetries are analyzed using twenty years of space-based Energy Balanced And Filled product of Clouds and the Earth's Radiant Energy System measurements. Despite surface asymmetries, top of the atmosphere temporally & hemispherically averaged albedo appears symmetric over Northern/Southern hemispheres. This is confirmed with the use of surrogate time-series, which fails to refute the hypothesis that the hemispheric albedo difference is distinguishable from zero. An analysis of reflected irradiance time-series fails to find any indicators of some dynamics enforcing this albedo symmetry. This analysis shows that variability in the reflected solar irradiance is almost entirely (99%) due to the seasonal (yearly and half yearly cycle) variations, mostly due to seasonal variations in insolation. Hemispheric residuals of the de-seasonalized reflected solar irradiance are not only small, but indistinguishable from noise, and thus not correlated across hemispheres. The residuals contain a global trend that is large, as compared to expected albedo feedbacks, and is also hemispherically symmetric. Neither the magnitude of these trends nor its symmetry – which could be indicative of a symmetry preserving cloud dynamics – is well understood. To pinpoint precisely which parts of the Earth system establish the hemispheric symmetry, we create an energetically consistent cloud-albedo field from the data. We show that the surface albedo asymmetry is compensated by asymmetries between clouds over extra-tropical oceans, with southern hemispheric storm-tracks being 11% cloudier than their northern hemisphere counterparts.

# Earth's albedo and its symmetry

George Datseris<sup>1</sup>, Bjorn Stevens<sup>1</sup>

<sup>1</sup>Max Planck Institute for Meteorology, Hamburg, Germany

## Key Points:

- Surrogate time-series analysis establishes the hemispheric albedo symmetry but fails to identify mechanisms enforcing this symmetry.
- Decadal trends in reflected insolation, while substantial, fail to break Earth's hemispheric albedo symmetry.
- Hemispheric clear-sky albedo asymmetries are balanced by hemispheric asymmetries in storm-track cloudiness.

---

Corresponding author: George Datseris, [george.datseris@mpimet.mpg.de](mailto:george.datseris@mpimet.mpg.de)

## Abstract

The properties of Earth’s albedo and its symmetries are analyzed using twenty years of space-based Energy Balanced And Filled product of Clouds and the Earth’s Radiant Energy System measurements. Despite surface asymmetries, top of the atmosphere temporally & hemispherically averaged albedo appears symmetric over Northern/Southern hemispheres. This is confirmed with the use of surrogate time-series, which fails to refute the hypothesis that the hemispheric albedo difference is distinguishable from zero. An analysis of reflected irradiance time-series fails to find any indicators of some dynamics enforcing this albedo symmetry. This analysis shows that variability in the reflected solar irradiance is almost entirely (99%) due to the seasonal (yearly and half yearly cycle) variations, mostly due to seasonal variations in insolation. Hemispheric residuals of the de-seasonalized reflected solar irradiance are not only small, but indistinguishable from noise, and thus not correlated across hemispheres. The residuals contain a global trend that is large, as compared to expected albedo feedbacks, and is also hemispherically symmetric. Neither the magnitude of these trends nor its symmetry – which could be indicative of a symmetry preserving cloud dynamics – is well understood. To pinpoint precisely which parts of the Earth system establish the hemispheric symmetry, we create an energetically consistent cloud-albedo field from the data. We show that the surface albedo asymmetry is compensated by asymmetries between clouds over extra-tropical oceans, with southern hemispheric storm-tracks being 11% cloudier than their northern hemisphere counterparts.

## Plain Language Summary

The planetary albedo is the portion of solar radiation reflected by the planet back to space, and is a prime factor deciding whether the planet will warm or cool over time. An intriguing property of the albedo is that, on average, Northern or Southern Hemisphere (NH or SH) have the same albedo, called hemispheric symmetry. The symmetry is surprising, because SH has much more ocean than land, and ocean is less reflective than land, so NH should have higher albedo. Nevertheless, clouds, which also tune the albedo, compensate the surface albedo imbalances of the two hemispheres, leading to an overall symmetric albedo. It is so far unclear how, or why, clouds perform this compensation. Here we show that this cloud compensation comes from the extra-tropical storm tracks of the SH, which are cloudier than those of the NH. We further analyze satellite radiation measurements in search of indicators of a process between NH and SH which establishes the albedo symmetry. While we find reflected radiation timeseries to be mostly a seasonal cycle superimposed with small noise, we also see that reflection decreases over-time with a significant trend that is identical for both hemispheres and thus hints at some interaction mechanism.

## 1 Introduction

The planetary albedo  $\alpha$ , an intrinsic property of a planet, measures the fraction of incident radiant energy (or insolation) that it reflects back to space. Its complement, the co-albedo  $(1-\alpha)$  thus determines what fraction of that insolation,  $I$ , remains to heat the planet. Several components of the planet and interactions among them go into deciding the value of  $\alpha$ . For Earth, the atmosphere and clouds are major contributors to albedo (Ramanathan, 1987), as are its surface properties (the land fraction, ice cover (Budyko, 1969) and even the biosphere (Betts, 2000)). Whereas the contributions of the constituent parts of the albedo have been studied in great detail, little attention has been devoted to understanding the properties of the albedo as a whole, as seen from space, and as one might do for another planet.

Clouds and Earth’s Radiant System (CERES) (Loeb et al., 2018; Kato et al., 2018) datasets provide precise measurements of Earth’s radiant energy balance as seen from

61 space. From these measurements it is possible to deduce the magnitude of Earth’s plan-  
 62 etary albedo,  $\alpha \approx 0.29$ , which varies surprisingly little across years (Stevens & Schwartz,  
 63 2012). Remarkably, the measurements show that on long-time averages the two hemi-  
 64 spheres have the same albedo, which we refer to as the *hemispheric albedo symmetry* (Stevens  
 65 & Schwartz, 2012; Voigt et al., 2013, 2014; Stephens et al., 2015, 2016; Haywood et al.,  
 66 2016; Bender et al., 2017). In the simplest approximation this arises from the asymmet-  
 67 ric response of clouds to surface albedo asymmetries (Voigt et al., 2013). As pointed out  
 68 by Stevens and Schwartz (2012) (see also the review by (Stephens et al., 2015)), these  
 69 properties of Earth’s albedo, while seemingly fundamental to an understanding of Earth’s  
 70 climate, lack even the outline of a theoretical explanation. Yet more remarkable is the  
 71 scarcity of work that attempts an explanation.

72 Early theoretical studies of Earth’s albedo mostly focused on surface contributions  
 73 to the planetary albedo, specifically the ice-albedo feedback first postulated by Arrhenius  
 74 (1896). Work on this question flourished in the early 1970s, see Budyko (1969); Sellers  
 75 (1969); North (1975); Chýlek and Coakley (1975); Stone (1978) among others. These stud-  
 76 ies sought to understand how the surface albedo depends on, and in turn influences, the  
 77 planetary temperature, but they did so by taking clouds for granted. In effect, they as-  
 78 sumed that, despite being by far the dominant and most dynamic component of the plan-  
 79 etary albedo (as later shown in pioneering work by Ramanathan (1987)), secular changes  
 80 in cloudiness are negligible. The early work also assumed, albeit implicitly, hemispheric  
 81 symmetry. Such an assumption seems natural, until one asks why clouds should vary be-  
 82 tween the hemispheres in a way that counterbalances a large,  $6 \text{ W m}^{-2}$ , surface radia-  
 83 tion asymmetry (see below), yet somehow be independent of a temporally changing cli-  
 84 mate state.

85 Our work is motivated by the intellectual tension that arises from the assumed con-  
 86 stancy of clouds over long timescales on one hand, and the fact that they compensate  
 87 the surface albedo asymmetry to result in overall symmetric albedo on the other hand.  
 88 We build upon earlier observational studies by Donohoe and Battisti (2011); Loeb et al.  
 89 (2019), who decomposed the TOA albedo value and time-anomalies into a surface and  
 90 atmosphere contribution, and by Voigt et al. (2013), who showed that the hemispheric  
 91 albedo symmetry is neither a trivial property of the Earth system, nor reproduced by  
 92 comprehensive Earth system models. By using the new cloud-information provided in  
 93 the latest release of CERES, we are able to create a new measure of cloudiness that al-  
 94 lows us to better understand how, and to what extent, cloud variations influence albedo  
 95 variations. Our analysis is further aided by more sophisticated methods of time-series  
 96 analysis, and a near doubling of the length of the observational record as compared to  
 97 what was available to Voigt et al. (2013). This allows a more rigorous quantification of  
 98 properties of Earth’s albedo that models or theories should explain, and provides con-  
 99 text for observations from an increasing number of studies of the albedo of other plan-  
 100 ets (Cowan & Agol, 2011; Shields et al., 2013; Mansfield et al., 2019), some of which also  
 101 identify a role for clouds (Kreidberg et al., 2014).

102 Our contributions are as follows. Using CERES data we show that the observed  
 103 hemispheric albedo symmetry is a statistically indistinguishable from a perfect symme-  
 104 try. This has been conjectured by previous studies, but not quantitatively demonstrated.  
 105 We further analyse radiation time-series in search of indicators of dynamical communi-  
 106 cation mechanisms that establish the symmetry between the two hemispheres. The over-  
 107 whelming majority of temporal variability is associated with the seasonal cycle. Resid-  
 108 uals of the seasonal cycle are found to be indistinguishable from noise and as such pro-  
 109 vide no sign of an extra-seasonal component to the albedo dynamics. Nor do we find ev-  
 110 idence in the radiation time-series record for an active process that maintains the hemi-  
 111 spheric albedo asymmetry. However, a long-term trend in the albedo is shown to be hemi-  
 112 spherically symmetric, which we would not expect in the absence such a process. We then  
 113 construct a “cloudiness” field, representing physical cloud albedo, which is a better rep-

**Table 1.** Notation used in this paper.

Symbol	Description	Type
$I$	insolation	$\text{W m}^{-2}$
$R$	all-sky refl. insolation at TOA	$\text{W m}^{-2}$
$K$	clear-sky refl. insolation at TOA	$\text{W m}^{-2}$
$Y$	Seasonal component of $R$	$\text{W m}^{-2}$
$\alpha$	all-sky albedo at TOA	fraction
$\alpha_K$	clear-sky albedo at TOA	fraction
$C$	Cloud albedo	fraction
$O$	ice-free ocean area fraction	fraction
$E$	ice & snow/ice coverage	fraction
$L$	ice-free land fraction	fraction
$\mathcal{T}$	time average (proper)	operation
$\mathcal{N}$	northern hemisphere average	operation
$\mathcal{S}$	southern hemisphere average	operation
$\mathcal{G}$	global average, $\equiv (\mathcal{S} + \mathcal{N})/2$	operation
$\mathcal{Z}$	zonal average	operation
NH, SH	northern, southern hemisphere	abbrv.

114 resentation of clouds’ impact on the shortwave part of the radiation balance than cloud  
115 fraction. Using this “cloudiness” we demonstrate that, as expected, the hemispheric albedo  
116 symmetry is a result of a hemispheric cloud asymmetry (see below). The cloudiness al-  
117 lows us to further demonstrate the extent to which average, versus spatiotemporal, cloud  
118 properties are responsible for observed cloud asymmetries. Unexpectedly we find that  
119 the major source of asymmetry is in the last place one would expect, over the ocean in  
120 the storm tracks, where the southern hemisphere is markedly more cloudy than the north-  
121 ern hemisphere, just enough so to exactly compensate the surface albedo asymmetry. In  
122 the conclusion section we discuss the potential impact of our work and the open ques-  
123 tions that remain.

## 124 Terminology

125 Notation and symbols used in the text are summarized in Table 1. The reference  
126 to clear-sky adopts values defined by CERES and is estimated from scenes identified as  
127 being cloud free. “All-sky” denotes no sub-sampling of specific scenes. The  $\approx$  symbol  
128 is used to indicate that a result has been rounded to the displayed digits, and the  $/$  de-  
129 notes a residual.

130 To account for the eccentricity of the Earth’s orbit, as well as the uneven sampling  
131 of the orbit done by monthly averages,  $\mathcal{T}$  weights every month by the number of days  
132 in that month. We additionally ensure that only full years (total time points multiple  
133 of 12) participate in the average. Not doing this can give wrong results. For example,  
134  $\mathcal{T}(\mathcal{N}(I)) - \mathcal{T}(\mathcal{S}(I)) \approx -0.002 \text{ W m}^{-2}$ , but using standard averaging of the first 240  
135 months (20 full years currently available in CERES EBAF) instead of weighted gives  $\approx$   
136  $-0.6 \text{ W m}^{-2}$ . Such large differences are reported in the literature, e.g. Fig. 4 of (Stephens  
137 et al., 2016), but are inconsistent with Kepler’s second law, which has the direct result  
138 that each hemisphere receives the same amount of total insolation over a full orbital pe-  
139 riod.

140 By definition,  $R = \alpha I$ , with  $\alpha$  the “albedo”. For the energy balance we mostly  
141 care about the portion of insolation that is scattered back to space, which we will call  
142 *effective albedo* and define as  $R/I$ . It can only be estimated when  $I \neq 0$ . We use the

143 term *physical albedo* to distinguish the case when  $\alpha$  is estimated in some other manner  
 144 like surface or optical properties, and thus can be defined also for the case  $I = 0$ .

## 145 2 Properties of the reflected insolation, $R$

### 146 2.1 Albedo's value and hemispheric symmetry

147 The effective albedo is  $\bar{\alpha} = \mathcal{G}(\mathcal{T}(R))/\mathcal{G}(\mathcal{T}(I)) \approx 0.291$ . For clear-sky we have  
 148  $\bar{\alpha}_K = \mathcal{G}(\mathcal{T}(K))/\mathcal{G}(\mathcal{T}(I)) \approx 0.156$ . Clouds thus increase the planetary albedo (on av-  
 149 erage) by almost a factor of two. The hemispheric difference in  $R$  is, on average,  $\mathcal{T}(\mathcal{N}(R)) -$   
 150  $\mathcal{T}(\mathcal{S}(R)) \approx 0.1 \text{ W m}^{-2}$ , which is 0.1% of the global average ( $\mathcal{T}(\mathcal{G}(R))$ ) and, as we will  
 151 show, indistinguishable from 0. The same difference for the clear-sky is  $\approx 6 \text{ W m}^{-2}$ , 11%  
 152 of its global average.

153 We adopt two approaches to test the hypothesis that  $\mathcal{T}(\mathcal{N}(R)) \neq \mathcal{T}(\mathcal{S}(R))$ . For  
 154 the first, we make use of surrogate time-series (Theiler et al., 1992; Lancaster et al., 2018)  
 155 to approximate  $\mathcal{N}(R)$  and  $\mathcal{S}(R)$ . To construct the surrogates we adopt the method of  
 156 Small et al. (2001), which is adapted to periodic data. The surrogates are constructed  
 157 from the data already contained in the signal, and are designed to have the same peri-  
 158 odic structure as the signal, but phase information is scrambled, destroying any corre-  
 159 lation between cycles. In essence the surrogates sub-sample the months with replacement  
 160 (i.e. for all Aprils, some are repeated in the surrogates, some are shuffled around, while  
 161 some others are skipped entirely). An example is shown in Fig. 1(a).

162 The hemispheric asymmetry of temporal averages of the surrogates, as estimated  
 163 from several thousand surrogates of  $\mathcal{N}(R)$  and  $\mathcal{S}(R)$ , gives a distribution of possible dif-  
 164 ferences. In Fig. 1(c) we compare this with the real difference, and find that a vanish-  
 165 ing (0) hemispheric asymmetry in the surrogate albedo is well within the 5-95% quan-  
 166 tiles of the data, establishing that the observed value indistinguishable from zero.

167 For the second approach, we decompose hemispherically averaged  $R$  into a com-  
 168 ponent  $Y$  containing the seasonal cycle and a residual  $R'_{\mathcal{N}} = \mathcal{N}(R) - Y_{\mathcal{N}}$  for NH, simi-  
 169 larly for SH, with the seasonal component defined as

$$170 \quad Y(t) = A_0 + \sum_i A_i \cos(2\pi\omega_i t + \phi_i), \quad (1)$$

171 with  $\omega_i$  the chosen frequencies of the decomposition. In our seasonal decomposition we  
 172 include only the annual (12 month) and semi-annual (6 month) cycle, as both arise from  
 173 the combination of Earth's obliquity and eccentricity. The fitting parameters,  $A_i, \phi_i$  are  
 174 estimated from the data, with  $A_0$  the time mean, following Bagge Carlson et al. (2017),  
 175 who transforms eq. (1) into a least squares problem in frequency space and works well  
 176 even for non-equi-spaced time axis. Our approach differs from the time anomaly decom-  
 177 position adopted by (Loeb et al., 2019) in that it makes the frequencies included in the  
 178 "seasonal" variations explicit, thereby allowing us to write  $Y(t)$  as an explicit function  
 179 of the *physical* time  $t$ .

180 Through the decomposition (1),  $A_{0,\mathcal{N}} = \mathcal{T}(\mathcal{N}(R))$ , likewise for the southern hemi-  
 181 sphere, hence  $\mathcal{T}(R'_{\mathcal{N}}) = \mathcal{T}(R'_{\mathcal{S}})$  by construction. To quantify how likely it is to observe  
 182 an asymmetry of  $0.1 \text{ W m}^{-2}$ , simply due to the fact that our measured residuals have  
 183 finite time length, we analyze  $D = R'_{\mathcal{N}} - R'_{\mathcal{S}}$ , where by definition  $\mathcal{T}(D) = 0 \text{ W m}^{-2}$ .  
 184 We model  $D$  as an auto-regressive process (Brockwell & Davis, 1996)

$$185 \quad D_t = \sum_{i=1}^M \theta_i D_{t-i} + \eta_t \quad (2)$$

186 with  $\eta$  white noise (with same standard deviation as  $D$ ),  $M$  the auto-regressive order  
 187 and  $\theta_i$  the parameter choices. Justification for this model is provided in §2.2. We esti-  
 188 mate the parameters  $\theta_i$  that best fit the measured time-series with the Levinson method

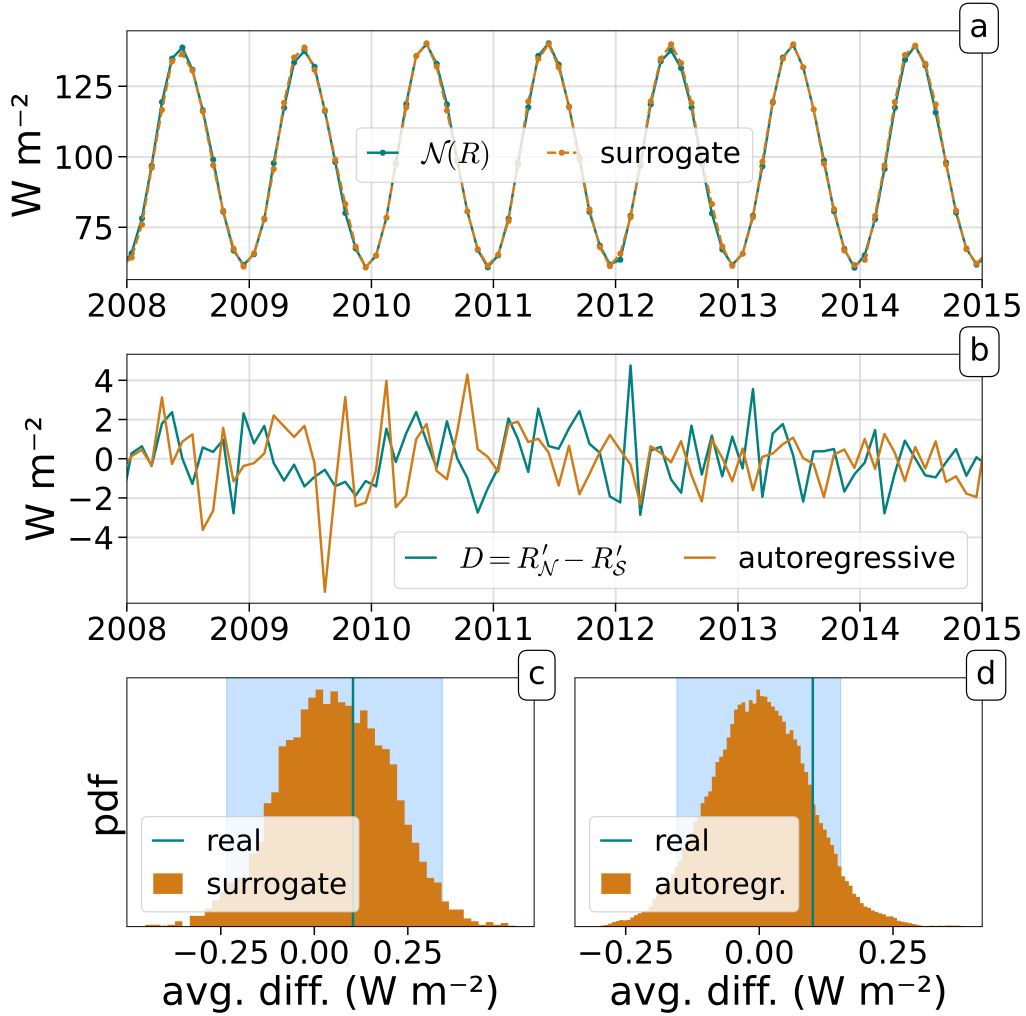


**Figure 1.** Hemispheric difference of  $R$  is indistinguishable from 0. (a) Hemispherically averaged  $R$ ,  $\mathcal{N}(R)$ , and pseudoperiodic surrogate which follows same dynamics. (b) Difference of residuals of hemispherically averaged  $R$  time-series, and an autoregressive process with same correlation structure. (c) Possible values of time-averaged hemispheric difference for pseudoperiodic surrogates. (d) Like (c), but now possible values come from sub-sampling 20 years of an infinitely long autoregressive realization. Blue rectangles show the 5-95% quantiles.

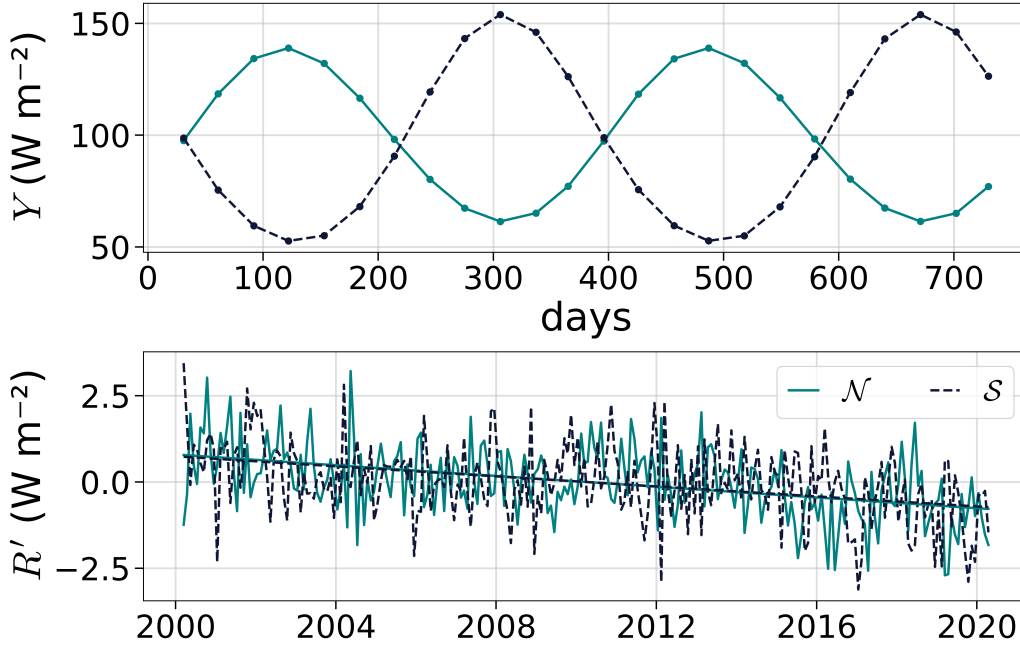


**Figure 2.** Seasonal decomposition of the reflected solar radiation  $R$ . The seasonal component  $s$  repeats identically for all time (and is plotted over days, because this time axis is used for the seasonal decomposition). Best line fit of the residuals is also plotted, and both hemispheres have a statistically significant trend of  $\approx -0.006 \text{ W m}^{-2}/\text{month} = 0.7 \text{ W m}^{-2}/\text{decade}$ .

189 of linear predictive code (Levinson, 1946), using  $M = 12$ . Fig. 1(b) presents  $D$  and  
 190 a realization of  $D_t$ . Using  $D_t$  we simulate a very long autoregressive time-series (that in  
 191 the limit  $t \rightarrow \infty$  has 0 mean by definition) and sample 242-long subsets of it and cal-  
 192 culate their mean. The resulting distribution is shown in Fig. 1(d). It shows that mea-  
 193 suring value  $0.1 \text{ W m}^{-2}$  simply because of finite time-span is a likely scenario.

194 The above analysis establishes the *hemispheric albedo symmetry*. This property of  
 195  $R$  was noted in the very first space-based measurements (Haar & Suomi, 1971), its sys-  
 196 tematic and quantitative study only became possible with the advent of the CERES data  
 197 (Stevens & Schwartz, 2012; Voigt et al., 2013, 2014; Stephens et al., 2015, 2016; Haywood  
 198 et al., 2016; Bender et al., 2017). Here we have shown that it is indistinguishable from  
 199 zero. For the present value of  $0.1 \text{ W m}^{-2}$  to prove significantly different from  $0 \text{ W m}^{-2}$ ,  
 200 would require the distribution of Fig. 1d to have a standard deviation of  $2\sigma \leq 0.1 \text{ W m}^{-2}$ .  
 201 This, we calculate, would require at least fifty years of data. In the following subsections  
 202 we analyze the radiation time-series further in search of an indication of dynamics, or  
 203 communication, that leads to the hemispheric albedo symmetry.

## 204 2.2 Dynamics of residuals

205 If there were some process that established the hemispheric albedo symmetry, we  
 206 might be able to identify it in the dynamics of  $R'_N$  and  $R'_S$ . For instance if one hemi-  
 207 sphere responded to internal anomalies that develop in the other hemisphere we would  
 208 expect to see this in the correlation structure between the two time-series. Fig. 2, presents  
 209  $Y$  and  $R'$ . The ratio  $\text{Var}(Y)/\text{Var}(R)$  is  $\approx 0.99$  for both NH and SH. With  $\sigma_{R'} \approx 1.1 \text{ W m}^{-2}$   
 210 for either hemisphere, very little signal is carried by the hemispheric residuals. Also, apart

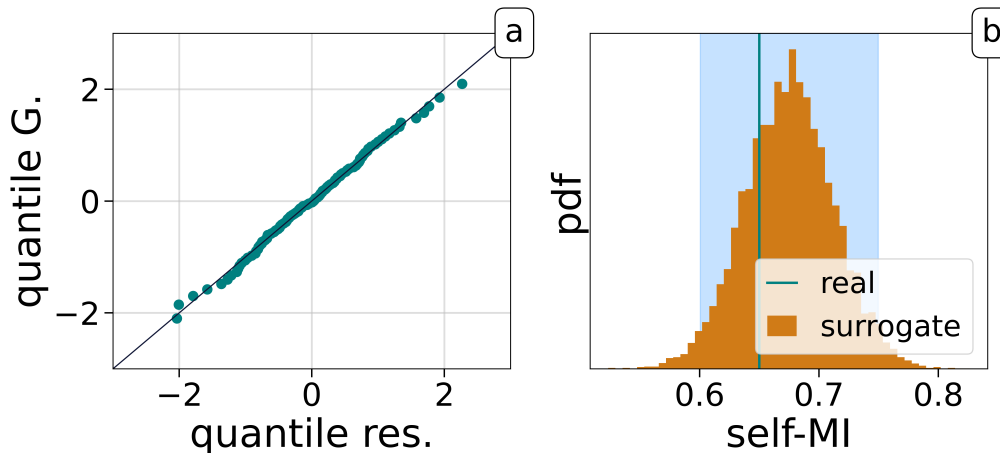


**Figure 3.** (a) A quantile-quantile plot of the quantile of the residuals versus the quantile of a Gaussian fitted to the residuals of NH. (b) Distribution of 1-step self-mutual-information of 10,000 truncated Fourier transform surrogates (see text), along with the value of the real time-series. Blue span shows the 5-95% quantiles of the distribution.

211 from a consistent downward trend in both hemispheres, no correlation exists between  
 212 the time-series of  $R'$  in the two hemispheres. Nor, as detailed next, could we detect such  
 213 relationships through a more quantitative analysis.

214 To test for the possibility of dynamics in the time series of  $R'$  we first try to reject  
 215 the null hypothesis that it can be described by a linear Gaussian (stochastic) process.  
 216 To do so we first compare the different quantiles of the data with those from a Gaussian  
 217 distribution fit to the same data. The result falls almost exactly on the diagonal (Fig. 3(a)),  
 218 which means that the original data can be modelled well from this distribution. Simi-  
 219 larly, but not shown, a K-sample Anderson-Darling test (Scholz & Stephens, 1987) also  
 220 fails to reject the null hypothesis. This establishes that the distribution of the data is  
 221 Gaussian, but not whether their sequence is correlated, or just noise.

222 To explore this latter question we create a surrogate time-series for  $R'_{\mathcal{N}}$  (we find  
 223 identical results for SH, not shown) following the approach of Nakamura et al. (2006),  
 224 which is designed to represent fluctuating data with constant trends. The surrogate fol-  
 225 lows a linear Gaussian process with autocorrelation the same as the input time-series,  
 226 and same trend, and thus satisfies the null hypothesis by construction (the autocorre-  
 227 lation uniquely defines a linear Gaussian process (Brockwell & Davis, 1996)). We then  
 228 attempt to distinguish this time-series from the actual time-series of  $R'_{\mathcal{N}}$ . To do so a 1-  
 229 step self-mutual-information statistic is adopted as a discriminatory statistic  $q$ . This quan-  
 230 tity is chosen as it has been shown to distinguish noise from determinism in small data  
 231 sets (Lancaster et al., 2018). The distribution of values  $p(q)$  can be constructed from dif-  
 232 ferent realizations of the surrogate. If the real data are significantly outside this distri-  
 233 bution, the null hypothesis can be rejected. As Fig. 3(b) shows, the real  $q$  is well within  
 234 the possible  $q$  of the null hypothesis (this is true for both NH and SH residuals), thus  
 235 failing to reject the null hypothesis. The apparent lack of dynamics in the residuals of  
 236 either hemisphere may simply be telling us that we have projected – through averaging  
 237 – a too high dimensional dynamics onto a too low dimensional space (and thus the re-  
 238 sult is indistinguishable from noise due to extreme information loss). To test for this pos-  
 239 sibility we repeated the above analysis on  $10^\circ \times 10^\circ$  longitude-latitude decompositions  
 240 and reached similar conclusions. On yet smaller scales, Voigt et al. (2013) showed that  
 241 albedo features become more strongly correlated with neighboring areas, and thus are

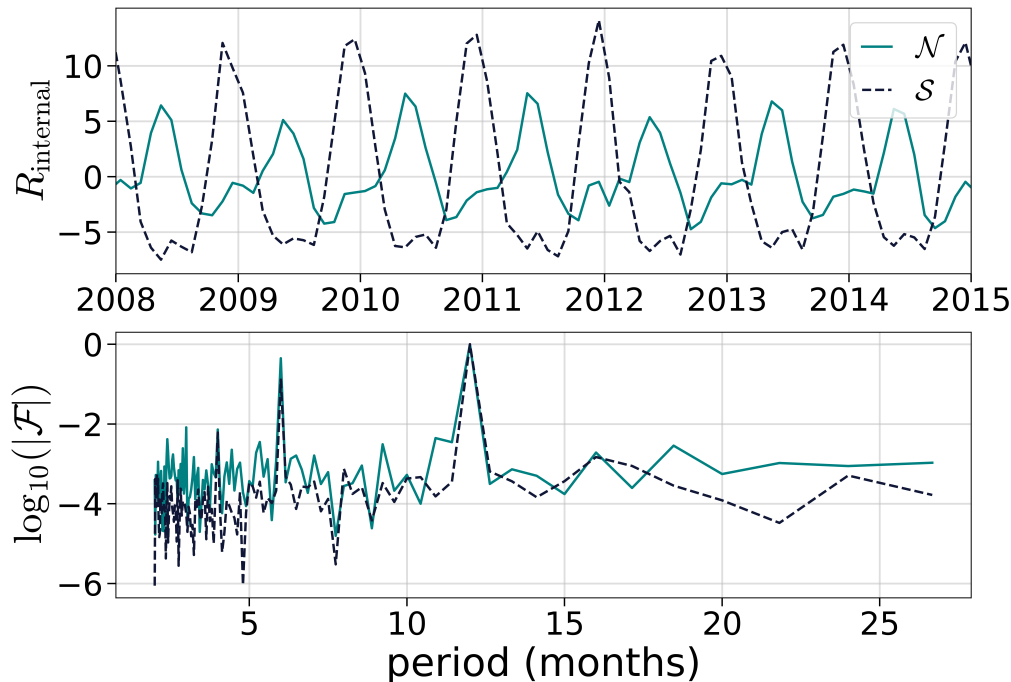


**Figure 4.** (a) Internal component of mean albedo decomposition of  $R$ . (b) Power spectrum of (a) (logarithm of absolute value of Fourier transform  $\mathcal{F}$ ).

242 no longer independent samples. A principle component analysis also failed to identify  
 243 dominant patterns of variability.

244 In summary, we were unable to identify any evidence of dynamics in the residual  
 245 time-series. Based on a variety of tests we could find no basis for distinguishing extra-  
 246 seasonal variations of  $R$  from noise. Given the strength of the trends in  $R'$  we find the  
 247 lack of signal in  $R'$  surprising.

### 248 2.3 Temporal variability

249 The seasonal decomposition as applied in Eq. (1) removes seasonal fluctuations of  
 250  $R$  that are due to seasonal fluctuations of physical albedo (e.g. the melting of ice dur-  
 251 ing summer) as well as those directly due to  $I$ . To separate the two effects we calculate  
 252 the temporal average value of  $\alpha$ ,  $\mathcal{T}(\alpha) = \mathcal{T}(R)/\mathcal{T}(I)$ , to then decompose  $R$  as  $R_{\text{solar}} =$   
 253  $\mathcal{T}(\alpha)I$  and  $R_{\text{internal}} = R - R_{\text{solar}}$  (this is done for each hemisphere, after hemispheric  
 254 averaging). For both hemispheres  $\mathcal{T}(\alpha) \approx 0.291$ . In essence,  $R_{\text{solar}}$  is the  $R$  we would  
 255 observe if we replaced Earth with a completely static, time-averaged version of itself.

256 Even in this decomposition, which disentangles the internal and solar fluctuations  
 257 (Fig. 4), the insolation accounts for most of the variability of  $R$ . Specifically for the NH,  
 258 84% of the variance of  $R$  is attributed to  $R_{\text{solar}}$ , only 1% to  $R_{\text{internal}}$  and 13% to their  
 259 co-variability. For the SH the numbers are 68%, 3% and 28%. A lack of power in Fourier  
 260 components other than those corresponding to the seasonal cycle (1 and 0.5 years, Fig. 4b)  
 261 in  $R_{\text{internal}}$  is consistent with our earlier analysis, which failed to distinguish  $R'$  from noise.

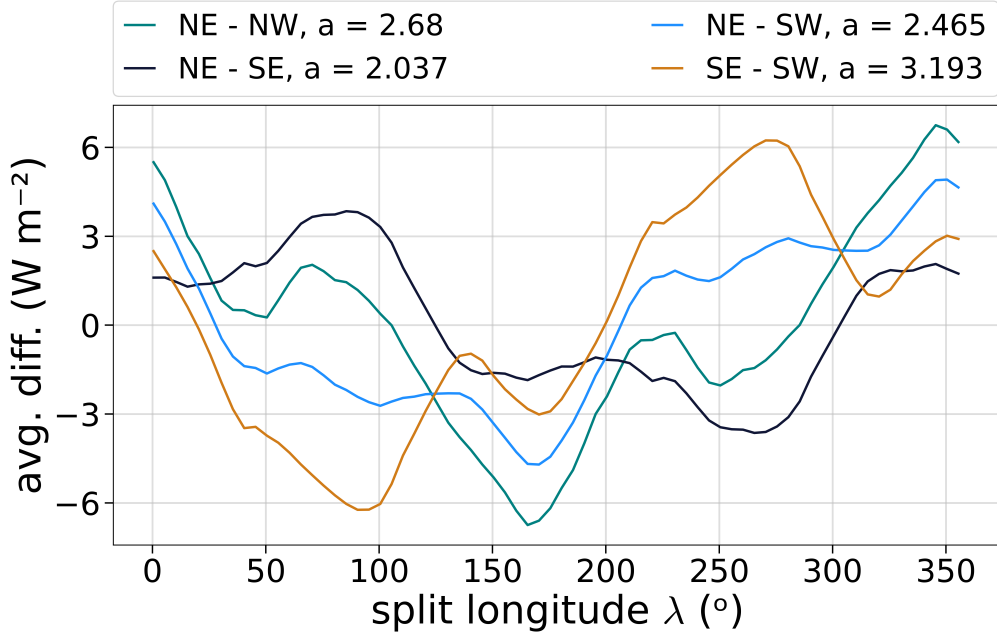


**Figure 5.**  $R$  is split into four quadrants at given longitude  $\lambda$ . The difference of the temporal & spatial averages between all four combinations of quadrants is plotted as a function of  $\lambda$ .  $a$  is the mean of the absolute value of each curve.

262

#### 2.4 Secular trends and hemispheric co-variances

263

264

265

266

267

268

The lack of signal in  $R'$  makes the magnitude of its secular trend surprising. From the best-fit of the residuals we estimate its magnitude to be  $0.7 \text{ W m}^{-2}$  per decade. Part of this can be explained by a trend  $\mathcal{G}(I)$ , which is thought to arise from the the 11-year solar cycle and the shortness of the CERES record, which began near a solar maximum and ends near a solar minimum. However the trend in  $\mathcal{G}(I)$  is only  $0.36 \text{ mW m}^{-2}$  per decade, hence  $\alpha\mathcal{G}(I)$  can only explain about 15% of the observed trend in  $\mathcal{G}(R')$ .

269

270

271

272

273

274

275

276

277

278

279

280

281

282

283

284

285

286

To develop a sense of the magnitude of the trend in  $\mathcal{G}(R')$ , we compare that part of its value not explained by the trend in  $\mathcal{G}(I)$  to roughly  $0.2 \text{ K}$  per decade rise in globally averaged surface temperatures since 2000. If the former were attributed to the latter it would imply a positive albedo feedback greater than  $0.7 \times (1 - 0.15) / 0.2 = 2.4 \text{ W m}^{-2} \text{ K}^{-1}$ . This is a factor of three or more larger than assessed values (Sherwood et al. (2020) report a central estimate of  $0.75 \text{ W m}^{-2} \text{ K}^{-1}$ ), which is to say it is a large number. The trend, first identified and analyzed by Loeb et al. (2020), was attributed to changes in north-eastern Pacific stratocumulus forced by decadal variations in sea-surface temperatures, in a way that models appear to largely capture. What hasn't been previously noted, and what we find difficult to explain given the lack of dynamics in  $R'$ , is why a trend in  $\mathcal{N}(R')$  attributed to changes in stratocumulus in the north-east pacific, is so well mirrored by much less spatially coherent (Loeb et al., 2020), but equal, changes in  $\mathcal{S}(R')$ . Were a substantial (more than a third) part of the observed trend attributable to global warming, it would have dramatic consequences. Put more broadly, if usefully quantifying the pace of global warming requires an ability to understand and quantify cloud responses to warming on the order of  $0.2 \text{ W m}^{-2} \text{ K}^{-1}$ , then surely more effort, building on prescient work by Loeb et al. (2020), to understand tenfold larger trends, and their symmetry, is warranted.

287 Despite our inability to distinguish detrended values of  $R'$  from noise, the similar-  
 288 ity of the trends in  $\mathcal{N}(R')$  and  $\mathcal{S}(R')$  makes a case for hemispheric communication. This  
 289 case is bolstered by an analysis of quadrants (semi-hemi-spheres). First, we perform a  
 290 simple analysis that shows that there is little evidence for a process operating on sub-  
 291 hemispheric scales that enforces a specific albedo value, which by chance is the same for  
 292 both hemispheres. For this we split each hemisphere into two halves (quadrants) sep-  
 293 arated by the great circle aligned with the longitude  $\lambda$ . We then calculate the average  
 294 difference of  $R$  between all six combinations of quadrants as a function of  $\lambda$ , (we present  
 295 only four, because due to the process scanning all  $\lambda \in [0, 360)$ , we get NE-SW  $\equiv$  NW-  
 296 SE and NE-SE  $\equiv$  NW-SW). Differences between arbitrary quadrants are, on average,  
 297 much (by more than an order of magnitude) larger than hemispheric differences as we  
 298 show in Fig. 5. However, differences between quadrants taken from different hemispheres  
 299 are robustly smaller than those taken from the same hemisphere. Albeit far from a rig-  
 300 orous proof, this is in line with what one would expect if there were some active method  
 301 of hemispheric albedo compensation.

### 302 3 Cloudiness and albedo

303 In this section we quantify the contribution of cloudiness to  $\alpha$  to investigate how  
 304 cloud asymmetries compensate hemispheric asymmetries in  $\alpha_K$ , the cloud-free albedo.

#### 305 3.1 Defining cloudiness, $C$

306 We begin by creating a “cloudiness” field  $C$  that represents physical cloud albedo  
 307 by combining two independent definitions of cloud albedo. These two definitions qual-  
 308 itatively agree with each other, and give us the confidence that our results do not de-  
 309 pend (qualitatively) on the exact definition of cloudiness. Combining them allows us to  
 310 take advantage of their differing properties: one is energetically consistent with  $I$  and  
 311  $R$ , the other can exist for  $I = 0$ .

312 The first definition for cloudiness is the *cloud contribution to atmosphere albedo*.  
 313 Donohoe and Battisti (2011) provide equations that can decompose the TOA albedo into  
 314 an additive contribution from the atmosphere and the surface, based on the radiative  
 315 fluxes at the TOA and surface and assuming that the atmosphere can be approximated  
 316 as a single, uniform layer described by a given albedo and transparency, having the same  
 317 scattering properties regardless if radiation comes from upwards or downwards. Loeb et  
 318 al. (2019) extended the model to decompose time anomalies. Here we use the same model  
 319 to decompose the planetary albedo into a surface (SFC) and atmosphere (ATM) contri-  
 320 butions  $\alpha = \alpha^{\text{ATM}} + \alpha^{\text{SFC}}$  and for clear-sky  $\alpha_K = \alpha_K^{\text{ATM}} + \alpha_K^{\text{SFC}}$  as described in §Appendix  
 321 A. These quantities allow us to define

$$322 C_\alpha = \alpha^{\text{CLD}} = \alpha^{\text{ATM}} - \alpha_K^{\text{ATM}}. \quad (3)$$

323 An advantage of  $C_\alpha$ , as compared to using the “cloud radiative effect” to define the clou-  
 324 diness (as  $(R - K)/I$ ), is that it does not conflate cloud with surface variability. Notice  
 325 that  $C_\alpha$  is effective and not physical albedo and is valid only for  $I \neq 0$ .

326 The second definition comes from a *cloud albedo parameterization* defined as

$$327 C_\tau = f \frac{\sqrt{3}(1-g)\tau}{2 + \sqrt{3}(1-g)\tau} \quad (4)$$

328 with  $f$  the cloud area fraction,  $\tau$  the cloud optical depth, and  $g$  the asymmetry factor  
 329 from the cloud particle phase function. Eq. (4) is the same as eq. (19) of Lacis and Hansen  
 330 (1974), but multiplied with  $f$ . CERES (MODIS) provides  $f$ , and  $\tau$ , but we have to es-  
 331 timate  $g$  (see below). The field  $\tau$  has missing values, at the high-latitudes of the win-  
 332 ter hemisphere. In Appendix A we describe a regularization process to fill these values.

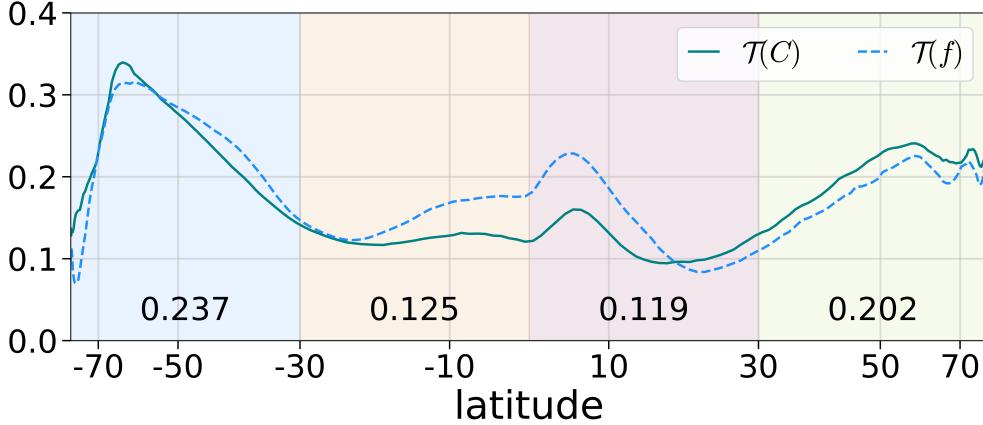


**Figure 6.** Temporally (and zonally) averaged cloudiness  $\mathcal{T}(\mathcal{Z}(C))$  and cloud area fraction  $f$  (normalized for same mean and std. as  $C$ ). We also display  $C$  averaged over four equal-area latitude zones (colored areas).

333 Using constant  $g = 0.9$  for all grid points already gives very good qualitative agreement  
 334 between  $C_\alpha, C_\tau$  in both temporally-averaged maps but also in spatially-averaged time-  
 335 series.

336 Choosing  $g$  so that  $\mathcal{T}(C_\tau - C_\alpha) = 0$  results in a physical cloud albedo,  $C_\tau$ , that  
 337 is energetically consistent with the time-averaged effective cloud albedo contribution,  $C_\alpha$ ,  
 338 everywhere, but at the expense of  $g$  varying spatially. Because the spatial variations are  
 339 small and within a physical range (see Appendix A), we adopt this approach, and de-  
 340 note the resultant cloud field by  $C$ . The reason for combining both definitions, by cre-  
 341 ating a spatially varying  $g$ , is that it allows us to define an energetically consistent cloud  
 342 field that is also defined when  $I = 0$ . In addition, by testing that our results are qual-  
 343 itatively similar for two independent definitions of cloud albedo gives confidence in their  
 344 robustness. For reference, temporally averaged maps of  $C, f, \tau, g$  are shown in Fig. A2.

### 345 3.2 Mean cloudiness

346 Temporally and zonally averaged distributions of  $C$  are presented in Fig. 6 and com-  
 347 pared to the cloud fraction  $f$  (normalized so that it has same mean and standard devi-  
 348 ation as  $C$ ). This shows that simply using  $f$  to represent cloudiness overestimates the  
 349 impact of clouds in the deep tropics (equatorward of about  $20^\circ$ ). As measured by  $C$ , the  
 350 tropics are substantially less cloudy than the extra-tropics. Additionally, despite large  
 351 latitudinal variations in cloud regimes – with the intra-tropical convergence zone being  
 352 mostly north of the equator –  $C$  varies little (by less than 15%) with latitude within the  
 353 tropics.

354 Hemispherically,  $\mathcal{T}(\mathcal{N}(C)) \approx 0.16$ , compared to  $\mathcal{T}(\mathcal{S}(C)) \approx 0.18$ . Hence the south-  
 355 ern hemisphere is cloudier by  $\approx 0.02$  – about 12% of the global average value. This asym-  
 356 metry in  $C$  is (see Fig. 6) largely a result of the SH extra-tropics being much cloudier  
 357 than the NH extra-tropics. This asymmetry is already evident in early cloud climatolo-  
 358 gies (Arrhenius, 1896; Brooks, 1927), its quantification here shows its importance for com-  
 359 pensating the hemispheric asymmetry of the surface albedo.

360 In principle, asymmetries in  $C$  need not imply asymmetries in the effective albedo  
 361 (and hence  $R$ ). For example, were the asymmetries carried by nocturnal cloudiness they  
 362 would have no effect on  $R$ . Qualitatively however, the asymmetry in cloudiness is suf-

363 sufficient to establish the hemispheric albedo symmetry (i.e. on first order the spatio-temporal  
 364 characteristics of  $C$  don't matter). Because the hemispheric difference of  $C$  represents  
 365 an effective albedo value, and because the clear-sky albedo difference is  $\delta\bar{\alpha}_K = \mathcal{T}(\mathcal{N}(K))/\mathcal{T}(\mathcal{N}(I)) -$   
 366  $\mathcal{T}(\mathcal{S}(K))/\mathcal{T}(\mathcal{S}(I)) \approx 0.02$ , then the hemispheric difference of  $C$  is sufficient to counter  
 367 that of  $K$ . Using the model of Donohoe and Battisti (2011), increasing the atmospheric  
 368 contribution to TOA albedo by 0.02 units gives a total TOA albedo increase of  $\approx 0.02$   
 369 for a wide range of choices of surface albedo, atmosphere albedo and atmosphere trans-  
 370 mittance. This does not prove that hemispheric differences in the mean cloudiness com-  
 371 pensate asymmetries in  $K$ , but suggests that it could.

### 372 3.3 Correlation with the solar cycle

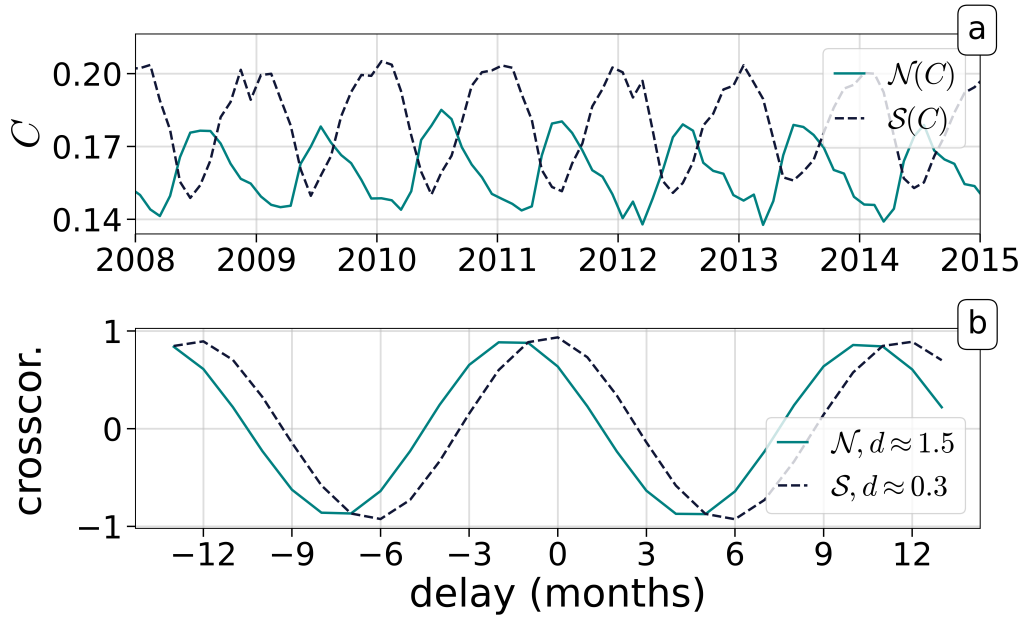


**Figure 7.** a: Cloudiness time-series, see eq. (4). A smaller time window is plotted for visual clarity. b: Temporal cross-correlation of  $C$  with  $I$  (for northern and southern hemispheric averages). The phase of the cross-correlations  $d$  is obtained by fitting  $\cos(\text{delay} + d)$  to the curves.

373 In addition to hemispheric differences in the temporal and spatially averaged cloudi-  
 374 ness, another candidate for compensating asymmetries in  $K$  is asymmetries in the co-  
 375 variability between  $I$  and  $C$ . In Fig. 7a we show hemispherically-averaged time-series of  
 376  $C$  and in Fig. 7b the cross-correlation function of the hemispherically averaged time-series  
 377 of cloudiness  $C$  and insolation  $I$ .  $C$  is strongly linearly correlated with  $I$  (maximum cross-  
 378 correlation values are  $\approx 1$ ), which is not surprising since cloudiness has a strong annual  
 379 cycle. What we did not expect is the different delays  $d$  in the maximum of the cross-correlation (which  
 380 is the phase shift between  $C$  and  $I$ ) between the two hemispheres.

381 For the SH  $C$  has its maximum approximately at the time of maximum insolation  
 382 as  $d \approx 0.3$  months is small. In the NH,  $d \approx 1.5$  months is larger, and appears to mostly  
 383 be attributable to clouds in the NH extra tropics (not shown), for reasons that remain  
 384 unclear. The larger lag of cloudiness in the NH contributes a small but measurable con-  
 385 tribution to the compensation of the clear-sky asymmetry. Shifting the cloudiness time-  
 386 series by 1.2 months (the difference of the delays between NH and SH), increases the cloud  
 387 reflection by  $\approx 0.28 \text{ W m}^{-2}$  – or about 10% of what is required to balance the asym-  
 388 metry in  $\alpha_K$ .

389

### 3.4 Cloudiness over different surface types

390

391

392

393

394

395

396

397

398

399

400

401

402

403

404

405

Having established that extra-tropical asymmetries in  $C$  largely compensate for hemispheric asymmetries in  $\alpha_K$ , here we ask whether these are predominantly associated with clouds over a particular type of surface. For instance, is the NH extra-tropics less cloudy by virtue NH land masses being less cloudy? We investigate this possibility by defining different surface types:  $O$  denotes the ice-free ocean area fraction,  $E$  the ice & snow coverage and  $L = 1 - O - E$  the ice-free land fraction. All three of these are spatiotemporal fields and  $O, E$  are accessible from CERES auxiliary datasets. To estimate cloudiness over the three different surface types here we use each one of  $O, E, L$  as statistical weights. For each point in time, and for each hemisphere, we perform a weighted spatial average (in addition to the standard weighting by area) of the field  $C$  with weight  $O, E$  or  $L$ . This gives us the average value of  $C$  over a specific surface type as a time-series. We then perform a temporal average  $\mathcal{T}$  and present the results in Fig. 8. Differences between the two hemispheres can be directly compared with the average hemispheric difference of  $C$  of  $\approx 0.02$ . Taking the co-variability of clouds and ice into account mostly impacts the results for  $C$  over ice, which makes sense given that  $E$  varies much more than  $L, O$ .

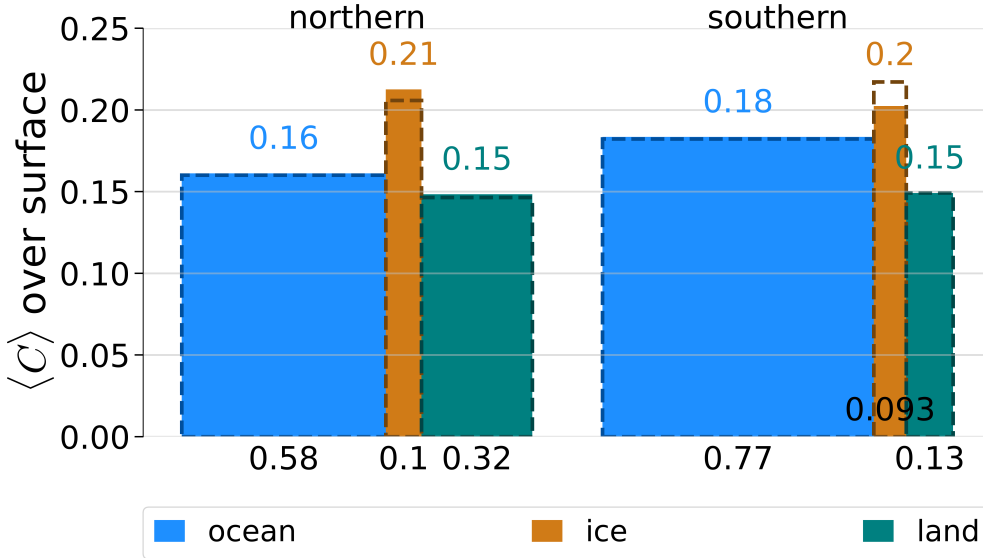


**Figure 8.** Average cloudiness  $C$  (height of the bars, also colored numbers) over different surface types. The width of the bars (also black numbers) is the surface fraction of that type. The dashed version of the bars is the numeric result of not taking co-variability of clouds and ice into account.

406

407

408

409

410

411

412

413

414

A trivial explanation for a compensating cloud contribution to the hemispheric clear-sky,  $\alpha_K$ , asymmetry would be that land is less cloudy than ocean, in a way that directly compensates for its reduced surface albedo relative to the ocean. Neglecting contributions from ice-covered surfaces, and given that the land fraction is  $\approx 19\%$  more in the NH than in the SH (Fig. 8), a 0.02 difference in  $C$  would require an  $C_O - C_L \approx 0.11$ . Fig. 8 shows that differences between  $C_L$  and  $C_O$  are much smaller than this. Instead the main difference between the cloudiness in the NH and that in the SH appears to be that the extra-tropical oceans of the SH are much cloudier than their counterpart in the NH (as seen by combining the information in Figs. 6 and 8).

## 4 Conclusions

We use twenty years of CERES data to study the global properties of Earth’s planetary albedo,  $\alpha$ . This quantity, which we define as the ratio of the reflected solar irradiance,  $R$ , to the insolation,  $I$ , is estimated as 0.291, consistent with many earlier estimates using the same, or similar data. The hemispheric albedo asymmetry, defined as the difference between the temporal and hemispheric averages of  $R$  is estimated as  $0.10(28) \text{ W m}^{-2}$ . The uncertainty (two sigma) is estimated using surrogate time-series and indicates that the measured asymmetry is indistinguishable from zero. In contrast, the hemispheric albedo asymmetry in the absence of clouds is a substantial fraction ( $6 \text{ W m}^{-2}$  or 11 %) of its global mean.

By constructing a quantitative measure of physical cloud albedo  $C$  we can decouple seasonality in clouds from those in insolation, and better quantify how cloud asymmetries compensate asymmetries in the cloud-free albedo to establish Earth’s hemispheric albedo symmetry. This analysis identifies the global tropics (equatorward of  $30^\circ$ ) as surprisingly transparent, with a zonally and temporally averaged value of  $C$  of 0.12 varying little with latitude. The extra-tropics are nearly twice as cloudy, the southern hemisphere (0.24) substantially more so than the northern hemisphere (0.20). Differences between cloudiness in the northern and southern hemispheres are primarily found over the ocean. Whereas land is less cloudy than the ocean (0.15 versus 0.17), the differences are insufficient to compensate for differences in land versus ocean clear-sky reflectances. Cloudiness in the northern hemisphere lags the annual cycle of insolation substantially more than in the southern hemisphere (1.5 months versus 0.3 months), which reduces the NH albedo. The effect is small ( $0.28 \text{ W m}^{-2}$ ) compared to surface albedo asymmetries. Where past work (Voigt et al., 2014) has investigated the role of shifts in tropical clouds as a means of symmetrizing the hemispheric albedo, the CERES data indicates that the asymmetry between the southern and northern hemispheric extra-tropical storm tracks is responsible for compensating hemispheric asymmetries in the cloud-free planetary albedo. The broad dynamical similarity between extra-tropical storms in the two hemispheres (Kodama et al., 2019) makes this difference in cloudiness unexpected. If anything, microphysical arguments would lead one to expect more ready rain initiation and less cloudiness in the southern hemisphere storms.

Analysis of the reflected flux,  $R$ , shows that almost all (97 % to 99 %, southern (SH) and northern (NH) respectively) of its variability can be explained by a seasonal cycle consisting of an annual and semi-annual harmonic. This seasonal cycle is mostly (68 % to 84 % SH/NH) attributable to the seasonal variations in insolation. The rest comes from seasonal variations in cloudiness. Extra-seasonal variations, defined as the residual  $R'$ , between  $R$  and its seasonal projection, are small ( $\sigma_{R'} = 1.1 \text{ W m}^{-2}$ ). Using a variety of methods from time-series analysis we are unable to distinguish the hemispheric residuals from noise, implying that they evolve independently of one another.

That the asymmetry in cloudiness counter-balancing the clear-sky albedo asymmetry is confined to clouds over the extra-tropical ocean would seem to argue against a hemispheric communication mechanism. At least were such a mechanism present we would have expected it to be associated with shifts in tropical rain bands, which modelling studies show are more closely associated with heat transport between the hemispheres (Kang et al., 2008). Further evidence against a dynamic mechanism that acts to symmetrise the hemispheric albedo is that there is so little signal of extra-seasonal variability in cloudiness, and that what signal there is, is indistinguishable from noise.

Given the lack of coherence, or correlated dynamics in the extra-seasonal component of  $R$  made the presence of a significant downward trend ( $-0.7 \text{ W m}^{-2}$  per decade) over the recorded period surprising. All the more surprising is that this trend, which previous literature has identified with a coherent mode of variability in north-east Pacific stratocumulus (Loeb et al., 2020), is almost identical in both hemispheres. This would

467 seem to argue for a dynamic mechanism which acts to maintain hemispheric albedo sym-  
 468 metry. An additional indicator of a possible mechanisms comes from an analysis of the  
 469 albedo of semi-hemispheres. It shows that the symmetry between semi-spheres selected  
 470 from different hemispheres is substantially greater than from semi-spheres within selected  
 471 from the same hemisphere.

472 If the observed trend in  $R$  were attributable to the changes in observed surface tem-  
 473 peratures, it would correspond to an exceptionally strong short-wave cloud feedback (greater  
 474 than  $2.4 \text{ W m}^{-2} \text{ K}^{-1}$ ) – enough to portend a run-away greenhouse effect. While we are  
 475 skeptical of this interpretation, the magnitude of the signal, and its coincidence with a  
 476 broader and unexplained pattern of cloudiness to be larger in the colder hemisphere, mer-  
 477 its attention.

## 478 Acknowledgments

479 We acknowledge Ulrich Parlitz and Hauke Schmidt for fruitful scientific discussions re-  
 480 garding this work.

481 **Data used and code base:** Analysis is based on the monthly averaged CERES  
 482 data. We use the Energy Balanced and Filled (EBAF) Ed. 4.1 (Loeb et al., 2018; Kato  
 483 et al., 2018), data set. For cloud properties we use the SYN1deg data (Doelling et al.,  
 484 2013; Rutan et al., 2015). We also use the auxiliary data of SYN1deg to get ice-free ocean  
 485 and ice & snow area fractions. All data have spatial resolution of  $1^\circ \times 1^\circ$  and span from  
 486 March 2000 to April 2020, totalling 242 months. All of these datasets are publicly avail-  
 487 able.

488 This work is also available as a fully reproducible code base [https://github.com/  
 489 Datseris/EarthAlbedoSymmetry](https://github.com/Datseris/EarthAlbedoSymmetry). The absolute exact data used in this paper are archived  
 490 in the same repository.

## 491 Appendix A Observational data processing for cloudiness

To derive the atmospheric and surface contributions to the albedo  $\alpha$  we re-write  
 the model of Donohoe and Battisti (2011) to obtain

$$\alpha^{\text{ATM}} = \frac{(\alpha - a_s t^2)}{1 - (a_s t)^2} \quad (\text{A1})$$

$$\alpha^{\text{SFC}} = \frac{a_s t^2 (1 - \alpha^{\text{TOA}} a_s)^2}{1 - \alpha^{\text{TOA}} a_s} \quad (\text{A2})$$

492 with  $\alpha = F_{\uparrow}^{\text{TOA}}/F_{\downarrow}^{\text{TOA}} \equiv R/I$  the planetary albedo,  $t = F_{\downarrow}^{\text{SFC}}/F_{\downarrow}^{\text{TOA}}$  the planetary  
 493 transmittance and  $a_s = F_{\uparrow}^{\text{SFC}}/F_{\downarrow}^{\text{SFC}}$  the surface albedo which in general is different than  
 494 the surface *contribution* to the planetary albedo due to further reflections between sur-  
 495 face and atmosphere.  $F$  simply stands for shortwave radiation, and all necessary instances  
 496 of  $F$  are provided in the same CERES dataset used throughout. Note that Stephens et  
 497 al. (2015) adopted a similar approach, but arrived at slightly different expressions, which  
 498 appear to be incorrect, or incorrectly typeset.

499 The optical depth field  $\tau$  provided by CERES has missing values in a large por-  
 500 tion of its time-series for spatial points near the poles. These missing values make hemi-  
 501 spheric averages impossible and thus need to be “fixed”. Here, we used a simple sinu-  
 502 soidal continuation, shown in Fig. A1. Using the same method as in §22.1, we fit sinu-  
 503 soidals of frequencies 1/year and 2/year to the available (i.e. non-missing) data. The value  
 504 of the sinusoidal fit is used to fill in only the entries of  $\tau$  that are missing. Furthermore,  
 505 Fig. A2 shows temporally averaged maps of  $C, f, \tau, g$ .

506 Different satellites and observational data products can have significant differences  
 507 in both how they define and measure cloud area fraction  $f$  and optical depth  $\tau$ , this will

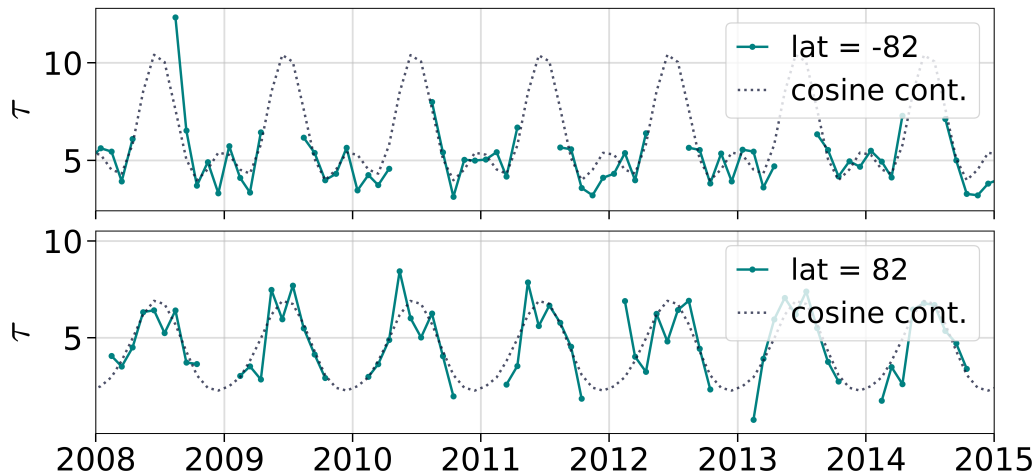


**Figure A1.** Continuation of the optical depth time-series  $\tau$ .

508 cause differences in the diagnosed values of  $g$  chosen to maintain consistency between  
 509  $C_\alpha$  and  $C$ .

## 510 References

- 511 Arrhenius, S. (1896, apr). On the influence of carbonic acid in the air upon the  
 512 temperature of the ground. *The London, Edinburgh, and Dublin Philosophical  
 513 Magazine and Journal of Science*, 41(251), 237–276. Retrieved from  
 514 <https://www.tandfonline.com/doi/full/10.1080/14786449608620846>  
 515 doi: 10.1080/14786449608620846
- 516 Bagge Carlson, F., Robertsson, A., & Johansson, R. (2017, 07). Linear parameter-  
 517 varying spectral decomposition. In *American control conference (acc),  
 518 2017* (pp. 146–151). Institute of Electrical and Electronics Engineers Inc.  
 519 Retrieved from [https://lup.lub.lu.se/search/ws/files/20192000/  
 520 LPVspectralestPaper.pdf](https://lup.lub.lu.se/search/ws/files/20192000/LPVspectralestPaper.pdf) doi: 10.23919/ACC.2017.7962945
- 521 Bender, F. A., Engström, A., Wood, R., & Charlson, R. J. (2017). Evaluation of  
 522 hemispheric asymmetries in marine cloud radiative properties. *Journal of Cli-  
 523 mate*, 30(11), 4131–4147. doi: 10.1175/JCLI-D-16-0263.1
- 524 Betts, R. A. (2000, November). Offset of the potential carbon sink from boreal  
 525 forestation by decreases in surface albedo. *Nature*, 408(6809), 187–190. Re-  
 526 trieved from <https://doi.org/10.1038/35041545> doi: 10.1038/35041545
- 527 Brockwell, P. J., & Davis, R. A. (1996). *Introduction to time series and forecast-  
 528 ing*. Springer New York. Retrieved from [https://doi.org/10.1007/978-1-  
 529 -4757-2526-1](https://doi.org/10.1007/978-1-4757-2526-1) doi: 10.1007/978-1-4757-2526-1
- 530 Brooks, C. (1927). The mean cloudiness over the Earth. *Mem. Roy. Meteorol. Soc.*,  
 531 1, 127–138.
- 532 Budyko, M. I. (1969). The effect of solar radiation variations on the climate of the  
 533 Earth. *Tellus*, 21(5), 611–619. doi: 10.3402/tellusa.v21i5.10109
- 534 Chýlek, P., & Coakley, J. A. (1975, apr). Analytical Analysis of a Budyko-Type Cli-  
 535 mate Model. *Journal of the Atmospheric Sciences*, 32(4), 675–679. Retrieved  
 536 from [http://journals.ametsoc.org/doi/abs/10.1175/1520-0469{  
 537 }281975{ }29032{ }3C0675{ }3AAAOABT{ }3E2.0.CO{ }3B2](http://journals.ametsoc.org/doi/abs/10.1175/1520-0469(1975)032%281975%29032%3C0675%3AAAOABT%3E2.0.CO%3B2) doi:  
 538 10.1175/1520-0469(1975)032%281975%29032%3C0675:AAOABT%2.0.CO;2
- 539 Cowan, N. B., & Agol, E. (2011, feb). THE STATISTICS OF ALBEDO AND

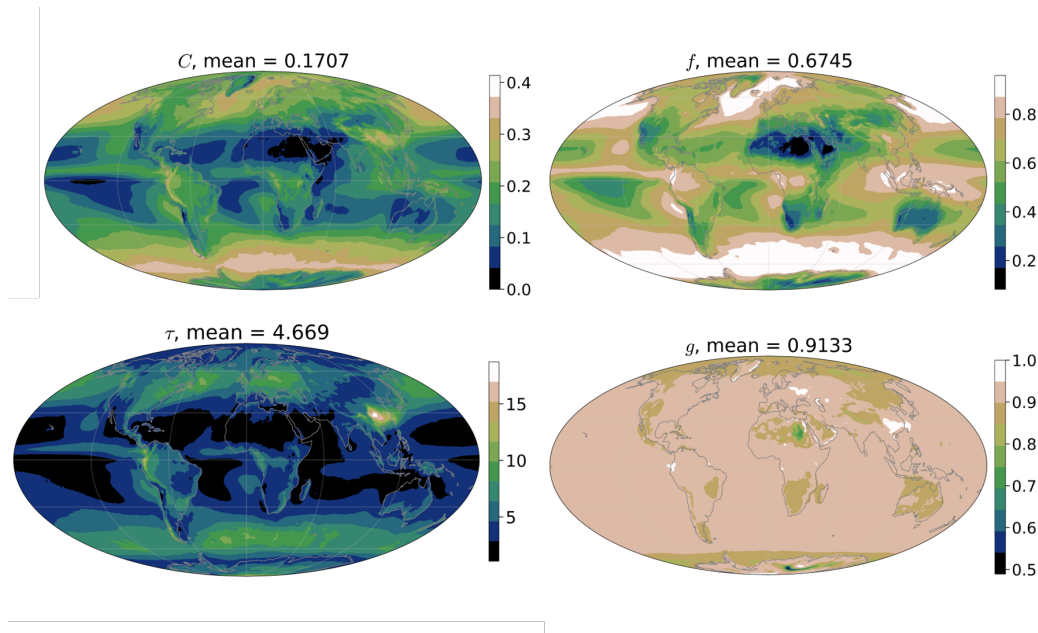


**Figure A2.** Temporally-averaged maps of fields used in the definition of effective cloud albedo, eq. (4). Shown also are the spatial means.

- 540 HEAT RECIRCULATION ON HOT EXOPLANETS. *The Astrophysical Journal*, 729(1), 54. Retrieved from <https://doi.org/10.1088/2043-9852/729/1/54>
- 541 doi: 10.1088/0004-637x/729/1/54
- 542 Doelling, D. R., Loeb, N. G., Keyes, D. F., Nordeen, M. L., Morstad, D., Nguyen, C., ... Sun, M. (2013, June). Geostationary enhanced temporal interpolation for CERES flux products. *Journal of Atmospheric and Oceanic Technology*, 30(6), 1072–1090. Retrieved from <https://doi.org/10.1175/jtech-d-12-00136.1> doi: 10.1175/jtech-d-12-00136.1
- 543
- 544
- 545
- 546
- 547
- 548 Donohoe, A., & Battisti, D. S. (2011). Atmospheric and surface contributions to planetary albedo. *Journal of Climate*, 24(16), 4402–4418. doi: 10.1175/2011JCLI3946.1
- 549
- 550
- 551 Haar, T. H. V., & Suomi, V. E. (1971, April). Measurements of the earth's radiation budget from satellites during a five-year period. part i: Extended time and space means. *Journal of the Atmospheric Sciences*, 28(3), 305–314. Retrieved from [https://doi.org/10.1175/1520-0469\(1971\)028<0305:moterb>2.0.co;2](https://doi.org/10.1175/1520-0469(1971)028<0305:moterb>2.0.co;2) doi: 10.1175/1520-0469(1971)028<0305:moterb>2.0.co;2
- 552
- 553
- 554
- 555
- 556 Haywood, J. M., Jones, A., Dunstone, N., Milton, S., Vellinga, M., Bodas-Salcedo, A., ... Stephens, G. (2016, January). The impact of equilibrating hemispheric albedos on tropical performance in the HadGEM2-ES coupled climate model. *Geophysical Research Letters*, 43(1), 395–403. Retrieved from <https://doi.org/10.1002/2015gl066903> doi: 10.1002/2015gl066903
- 557
- 558
- 559
- 560
- 561 Kang, S. M., Held, I. M., Frierson, D. M. W., & Zhao, M. (2008, July). The Response of the ITCZ to Extratropical Thermal Forcing: Idealized Slab-Ocean Experiments with a GCM. *Journal of Climate*, 21(14), 3521–3532. doi: 10.1175/2007JCLI2146.1
- 562
- 563
- 564
- 565 Kato, S., Rose, F. G., Rutan, D. A., Thorsen, T. J., Loeb, N. G., Doelling, D. R., ... Ham, S.-H. (2018, May). Surface irradiances of edition 4.0 clouds and the earth's radiant energy system (CERES) energy balanced and filled (EBAF) data product. *Journal of Climate*, 31(11), 4501–4527. Retrieved from
- 566
- 567
- 568

- 569 <https://doi.org/10.1175/jcli-d-17-0523.1> doi: 10.1175/jcli-d-17-0523.1  
570 Kodama, C., Stevens, B., Mauritsen, T., Seiki, T., & Satoh, M. (2019). A  
571 New Perspective for Future Precipitation Change from Intense Extratrop-  
572 ical Cyclones. *Geophysical Research Letters*, *46*(21), 12435–12444. doi:  
573 10.1029/2019GL084001
- 574 Kreidberg, L., Bean, J. L., Désert, J. M., Benneke, B., Deming, D., Stevenson,  
575 K. B., ... Homeier, D. (2014). Clouds in the atmosphere of the super-Earth  
576 exoplanet GJ 1214b. *Nature*, *505*(7481), 69–72. doi: 10.1038/nature12888
- 577 Lacis, A. A., & Hansen, J. (1974, jan). A Parameterization for the Absorption of So-  
578 lar Radiation in the Earth’s Atmosphere. *Journal of the Atmospheric Sciences*,  
579 *31*(1), 118–133. Retrieved from [http://journals.ametsoc.org/doi/abs/  
580 10.1175/1520-0469\(1974\)031\(0118:APFTAO\)2.0.CO;2](http://journals.ametsoc.org/doi/abs/10.1175/1520-0469(1974)031(0118:APFTAO)2.0.CO;2)  
581 .0.CO(1974)031(0118:APFTAO)2.0.CO;2  
582 Lancaster, G., Iatsenko, D., Pidde, A., Ticcinelli, V., & Stefanovska, A. (2018). Sur-  
583 rogate data for hypothesis testing of physical systems. *Physics Reports*, *748*,  
584 1–60. Retrieved from <https://doi.org/10.1016/j.physrep.2018.06.001>  
585 doi: 10.1016/j.physrep.2018.06.001
- 586 Levinson, N. (1946, April). The wiener (root mean square) error criterion in fil-  
587 ter design and prediction. *Journal of Mathematics and Physics*, *25*(1-4), 261–  
588 278. Retrieved from <https://doi.org/10.1002/sapm1946251261> doi: 10  
589 .1002/sapm1946251261
- 590 Loeb, N. G., Doelling, D. R., Wang, H., Su, W., Nguyen, C., Corbett, J. G., ...  
591 Kato, S. (2018, January). Clouds and the earth’s radiant energy system  
592 (CERES) energy balanced and filled (EBAF) top-of-atmosphere (TOA)  
593 edition-4.0 data product. *Journal of Climate*, *31*(2), 895–918. Retrieved from  
594 <https://doi.org/10.1175/jcli-d-17-0208.1> doi: 10.1175/jcli-d-17-0208.1
- 595 Loeb, N. G., Wang, H., Allan, R., Andrews, T., Armour, K., Cole, J. N. S., ...  
596 Wyser, K. (2020). New Generation of Climate Models Track Recent Un-  
597 precedented Changes in Earth’s Radiation Budget Observed by CERES.  
598 *Geophysical Research Letters*, *n/a*(n/a), e2019GL086705. Retrieved from  
599 <https://doi.org/10.1029/2019GL086705> doi: 10.1029/2019GL086705
- 600 Loeb, N. G., Wang, H., Rose, F. G., Kato, S., Smith, W. L., & Sun-Mack, S. (2019).  
601 Decomposing shortwave top-of-atmosphere and surface radiative flux variations  
602 in terms of surface and atmospheric contributions. *Journal of Climate*, *32*(16),  
603 5003–5019. doi: 10.1175/JCLI-D-18-0826.1
- 604 Mansfield, M., Kite, E. S., Hu, R., Koll, D. D. B., Malik, M., Bean, J. L., & Kemp-  
605 ton, E. M.-R. (2019, dec). Identifying atmospheres on rocky exoplanets  
606 through inferred high albedo. *The Astrophysical Journal*, *886*(2), 141. Re-  
607 trieved from <https://doi.org/10.3847/1538-4357/ab4c90> doi:  
608 10.3847/1538-4357/ab4c90
- 609 Nakamura, T., Small, M., & Hirata, Y. (2006, Aug). Testing for nonlinearity in ir-  
610 regular fluctuations with long-term trends. *Phys. Rev. E*, *74*, 026205. Re-  
611 trieved from <https://link.aps.org/doi/10.1103/PhysRevE.74.026205> doi:  
612 10.1103/PhysRevE.74.026205
- 613 North, G. R. (1975). *Theory of Energy-Balance Climate Models* (Vol. 32) (No. 11).  
614 doi: 10.1175/1520-0469(1975)032(2033:TOEBCM)2.0.CO;2
- 615 Ramanathan, V. (1987). The role of earth radiation budget studies in climate and  
616 general circulation research. *Journal of Geophysical Research*, *92*(D4), 4075.  
617 doi: 10.1029/jd092id04p04075
- 618 Rutan, D. A., Kato, S., Doelling, D. R., Rose, F. G., Nguyen, L. T., Caldwell,  
619 T. E., & Loeb, N. G. (2015, June). CERES synoptic product: Methodol-  
620 ogy and validation of surface radiant flux. *Journal of Atmospheric and Oceanic*  
621 *Technology*, *32*(6), 1121–1143. Retrieved from [https://doi.org/10.1175/  
622 jtech-d-14-00165.1](https://doi.org/10.1175/jtech-d-14-00165.1) doi: 10.1175/jtech-d-14-00165.1
- 623 Scholz, F. W., & Stephens, M. A. (1987, September). K-sample anderson-darling

- 624 tests. *Journal of the American Statistical Association*, 82(399), 918. Retrieved  
 625 from <https://doi.org/10.2307/2288805> doi: 10.2307/2288805
- 626 Sellers, W. D. (1969). *Global Climatic Model Based on the Energy Balance of the*  
 627 *Earth- Atmosphere System* (Vol. 8) (No. 3).
- 628 Sherwood, S., Webb, M. J., Annan, J. D., Armour, K. C., Forster, P. M., Harg-  
 629 reaves, J. C., ... Zelinka, M. D. (2020). An assessment of Earth's climate  
 630 sensitivity using multiple lines of evidence. *Reviews of Geophysics*. doi:  
 631 10.1029/2019RG000678
- 632 Shields, A. L., Meadows, V. S., Bitz, C. M., Pierrehumbert, R. T., Joshi, M. M.,  
 633 & Robinson, T. D. (2013, August). The effect of host star spectral energy  
 634 distribution and ice-albedo feedback on the climate of extrasolar planets.  
 635 *Astrobiology*, 13(8), 715–739. Retrieved from [https://doi.org/10.1089/](https://doi.org/10.1089/ast.2012.0961)  
 636 [ast.2012.0961](https://doi.org/10.1089/ast.2012.0961) doi: 10.1089/ast.2012.0961
- 637 Small, M., Yu, D., & Harrison, R. G. (2001). Surrogate test for pseudoperiodic time  
 638 series data. *Physical Review Letters*, 87(18), 188101–1–188101–4. doi: 10.1103/  
 639 PhysRevLett.87.188101
- 640 Stephens, G. L., Hakuba, M. Z., Hawcroft, M., Haywood, J. M., Behrangi, A., Kay,  
 641 J. E., & Webster, P. J. (2016). The Curious Nature of the Hemispheric Sym-  
 642 metry of the Earth's Water and Energy Balances. *Current Climate Change*  
 643 *Reports*, 2(4), 135–147. Retrieved from [http://dx.doi.org/10.1007/](http://dx.doi.org/10.1007/s40641-016-0043-9)  
 644 [s40641-016-0043-9](http://dx.doi.org/10.1007/s40641-016-0043-9) doi: 10.1007/s40641-016-0043-9
- 645 Stephens, G. L., O'Brien, D., Webster, P. J., Pilewski, P., Kato, S., & Li, J.-l. (2015,  
 646 mar). The albedo of Earth. *Reviews of Geophysics*, 53(1), 141–163. Re-  
 647 trieved from <http://doi.wiley.com/10.1002/2014RG000449> doi: 10.1002/  
 648 2014RG000449
- 649 Stevens, B., & Schwartz, S. E. (2012). Observing and Modeling Earth's Energy  
 650 Flows. *Surveys in Geophysics*, 33(3-4), 779–816. doi: 10.1007/s10712-012-9184-  
 651 0
- 652 Stone, P. H. (1978). Constraints on dynamical transports of energy on a spherical  
 653 planet. *Dynamics of Atmospheres and Oceans*, 2(2), 123–139. doi: 10.1016/  
 654 0377-0265(78)90006-4
- 655 Theiler, J., Eubank, S., Longtin, A., Galdrikian, B., & Doyne Farmer, J. (1992).  
 656 Testing for nonlinearity in time series: the method of surrogate data. *Physica*  
 657 *D: Nonlinear Phenomena*, 58(1-4), 77–94. doi: 10.1016/0167-2789(92)90102-  
 658 S
- 659 Voigt, A., Stevens, B., Bader, J., & Mauritsen, T. (2013). The observed hemispheric  
 660 symmetry in reflected shortwave irradiance. *Journal of Climate*, 26(2), 468–  
 661 477. doi: 10.1175/JCLI-D-12-00132.1
- 662 Voigt, A., Stevens, B., Bader, J., & Mauritsen, T. (2014). Compensation of hemi-  
 663 spheric albedo asymmetries by shifts of the ITCZ and tropical clouds. *Journal*  
 664 *of Climate*, 27(3), 1029–1045. doi: 10.1175/JCLI-D-13-00205.1